An Assessment of Solar Irradiance Enhancement events during CyCARE campaign at Limassol, Cyprus

Konstantinos Fragkos[1]*, Ilias Fountoulakis[3,4], Georgia Charalampous[1,2], Kyriakoula Papachristopoulou[3], Rodanthi-Elisavet Mamouri[1,2], Dragos Ene[1], Argyro Nisantzi[1,2], Albert Ansmann[5], Patric Seifert[5], Diofantos Hadjimitsis[1,2], and Stelios Kazadzis[6]

(1) Department of Resilient Society /Department of Environment and Climate Eratosthenes Centre of Excellence, Fragklinou Rousvelt 82, 3012 Limassol, Cyprus,

(2) Department of Civil Engineering & Geomatics, Cyprus University of Technology, 3036 Limassol, Cyprus,

(3) Institute for Astronomy, Astrophysics, Space Applications and Remote Sensing, National Observatory of Athens (IAASARS/NOA), GR15236 Athens, Greece,

(4) Research Centre for Atmospheric Physics and Climatology, Academy of Athens, 106 79 Athens, Greece,

(5) Leibniz Institute for Tropospheric Research, Leipzig, Germany,

(6) Physikalisch-Meteorologisches Observatorium Davos, World Radiation Center (PMOD/WRC), Davos 7260, Switzerland

ABSTRACT

Solar irradiance enhancement events, particularly under broken cloud conditions, can affect the Earth's energy balance and have direct implications for solar energy production and climate modeling. The ability to accurately quantify and understand these events can significantly contribute to improving our understanding of cloud-radiation interactions and, by extension, regional and global climate predictions.

The Cyprus Aerosol and Cloud Experiment (CyCARE) campaign was an effort to elucidate aerosol-cloud interactions under the distinct dust and aerosol pollution conditions of the Middle East. Conducted in Limassol, Cyprus, from October 2016 to April 2018, as a collaborative endeavor between the Cyprus University of Technology (CUT) and the Leibniz Institute for Tropospheric Research (TROPOS). Utilizing the Leipzig Aerosol and Cloud Remote Observations System (LACROS) — a suite comprising both active and passive remote sensing instruments — the campaign facilitated an unprecedented collection of atmospheric data. Among these instruments, the Polly^{XT} Raman-polarization lidar, 35-GHz cloud radar, disdrometer, Doppler wind-lidar, and microwave radiometer have been instrumental in capturing the vertical aerosol distribution, cloud microphysical properties, precipitation patterns, aerosol and cloud dynamics. A noteworthy aspect of the Cy-CARE campaign is the integration of the MObile RaDiation ObseRvatory (MORDOR) from June 2017, enhancing the measurement capabilities with a Class A pyranometer in compliance with ISO 9060:2018 standards for global horizontal irradiance monitoring.

This study specifically aims to assess solar irradiance enhancement events attributable to broken cloud conditions observed during the Cy-CARE campaign. Leveraging the clear sky shortwave irradiance simulations from the radiative transfer package libRadtran, the research identifies and examines these enhancement events. Ancillary measurements of cloud evolution and microphysical parameters, courtesy of LACROS, furnish detailed insights into the cloud types instrumental in these enhancements.

Keywords: Cloud Enhancement, Solar Irradiance, Clear sky modelling

1. INTRODUCTION

Clouds play a very important role in modulating solar irradiance at the Earth's surface, acting mainly as attenuators and, under certain conditions, enhancers of solar radiation. The phenomenon of cloud-induced enhancement of solar irradiance, known as cloud enhancement events (CEEs), presents a paradoxical scenario where solar irradiance exceeds clear sky

Tenth International Conference on Remote Sensing and Geoinformation of the Environment (RSCy2024), edited by A. Christofe, S. Michaelides, D. Hadjimitsis, C. Danezis, K. Themistocleous, N. Kyriakides, G. Schreier,
Proc. of SPIE Vol. 13212, 1321206 · © 2024 SPIE · 0277-786X · doi: 10.1117/12.3034290

levels under broken cloud conditions[1]. These events, beyond their scientific intrigue, have implications for the operation and efficiency of solar photovoltaic (PV) plants[2,3]. As evidenced by recent studies, CEEs can lead to operational disruptions and economic losses in PV plants due to power clipping, tripping of protection elements[4]. Additionally, they lead to increased UV radiation exposure[5]. The importance of these phenomena extends to the fields of climate science and renewable energy management, prompting a need for comprehensive analysis to inform both meteorological understanding and PV plant design.

The current study aims to dissect the dynamics of CEEs within the coastal context of Limassol, Cyprus, through an extensive analysis of solar irradiance data collected over eight months as part of the CyCARE (Cyprus Cloud Aerosol and Radiation Experiment) campaign[6]. The CyCARE campaign, conducted in Limassol, serves as the backdrop for this investigation. This section of the Mediterranean has been identified as a critical area for studying cloud dynamics due to its unique atmospheric conditions[7]. The campaign's objective, methodology, and preliminary findings underscore the importance of regional studies in advancing our global understanding of solar irradiance variability.

This paper is organized as follows: Section 2 details the methodology, including an overview of the CyCARE campaign (2.1), the instrumentation used (2.2), the clear sky model for CEE detection (2.3), and the analytical methods employed (2.4). Section 3 presents the results, divided into an evaluation of the clear sky model under identified conditions (3.1), the identification of CEEs (3.2), and statistical analyses of their frequency (3.3). Finally, Section 4 synthesizes the main conclusions drawn from the study.

2. DATA AND METHODOLOGY

2.1 CyCARE campaign

The CyCARE (Cyprus Cloud Aerosol and Radiation Experiment) campaign represents a significant collaborative effort between the Cyprus University of Technology (CUT) and the Leibniz Institute for Tropospheric Research (TROPOS), aimed at advancing our understanding of aerosol-cloud dynamics and interactions under the unique atmospheric conditions prevalent in the East Mediterranean, north Africa and the Middle East (EMMENA region). Conducted in Limassol, Cyprus (34.675° N, 33.04° E, 22 m asl), the campaign spanned from October 2016 to April 2018. This initiative was particularly focused on examining the dynamics of dust and aerosol pollution and their influence on cloud formation and properties—an area of research critical for elucidating the complex feedback mechanisms affecting regional and global climate patterns.

A key aspect of the CyCARE campaign was the deployment of the Leipzig Aerosol and Cloud Remote Observations System (LACROS) at the premises of CUT. The LACROS setup is a comprehensive suite of both active and passive remote-sensing instruments designed to capture a multidimensional picture of atmospheric aerosols and clouds. Among the instruments included were a Polly^{XT} Raman-polarization lidar to retrieve aerosol vertical distribution, a 35-GHz cloud radar to obtain cloud microphysical properties, a disdrometer to measure precipitation, a Doppler wind lidar to track aerosol and cloud dynamics, and a microwave radiometer to measure water vapor and liquid water content.

Furthermore, the TROPOS mobile radiation observatory (MORDOR) complemented the observational capabilities of LACROS by conducting radiation measurements between June 2017 and January 2018. These measurements were integral for quantifying the direct and indirect effects of aerosols and clouds on solar radiation.

2.2 Instrumentation

The instrumentation deployed as part of the MORDOR setup in Limassol was chosen to ensure the high accuracy and reliability of solar irradiance measurements. Central to this setup were two Class A instruments, as classified by ISO 9060:2018 standards, provided by EKO Instruments. These included:

- Pyranometer (Model MS-80): Utilized for measuring global horizontal irradiance (GHI), this instrument is renowned for its precision and durability. The MS-80's design minimizes thermal offsets and offers an estimated measurement uncertainty of about 2% under clear sky conditions, making it highly suitable for capturing subtle variations in solar irradiance.
- Pyrheliometer (Model MS-56): This instrument was employed to measure direct normal irradiance (DNI). Similar to the pyranometer, the MS-56 is a Class A instrument, reflecting its high measurement accuracy and reliability.

Additionally, to complement these irradiance measurements, a fish-eye camera (Model Vivotek FE8172V) was used to capture sky images every 10 minutes from sunrise to sunset. These images are invaluable for visual assessments of sky conditions, cloud coverage, facilitating a more comprehensive analysis of solar irradiance data.

2.3 Clear sky model

For the analysis of clear sky conditions, simulations of clear sky irradiance were conducted daily throughout the period from June 2017 to January 2018. These simulations employed a 15-minute timestep, with results interpolated to a 1-minute resolution to align closely with the temporal frequency of the measurements. The core of these calculations was the utilization of precalculated look-up tables (LUTs), a strategic choice to enhance computational efficiency.
These LUTs contain simulated solar surface radiation (SSR) values generated using the libRadtran radiative transfer package (RTM)[8]. Simulations were performed for a range of solar zenith angles (SZAs) and atmospheric parameters representative of cloudless conditions, thereby facilitating accurate estimates of clear sky irradiance. Given that this modeling approach, including the specific parameters and setup, has been previously detailed in the literature, here we will not reiterate those specifics. For a comprehensive understanding of the model's configuration and the parameters employed, readers are directed to the work of Fountoulakis et al.[9], where these elements are exhaustively described.

2.4 Analysis methods

The first criterion is that the elevation of the sun must be above 10 degrees. The second criterion requires the measured irradiance to be higher than the corresponding clear sky value, and the third insists that the sun-disc should not be obscured by clouds.

To accurately determine the occurrence of CEE, we initiated our investigation by evaluating the performance of our chosen clear sky model. This initial step is very important, as it aids in establishing an appropriate threshold for modeled clear sky irradiances. Exceeding this threshold with measured irradiances is indicative of an enhancement, thereby characterizing CEE. For the identification of clear sky periods within our dataset, we employed the method developed by Inman et al.[10], adapted for MATLAB by Jamie Bright[11]. This model's reliance solely on GHI and DNI measurements, alongside their respective clear sky estimates, renders it particularly suitable for our study's context, where additional data types (e.g., diffuse irradiance) are not available. The model's applicability in data-limited scenarios, coupled with its demonstrated accuracy in pinpointing clear sky conditions, underscored its selection for our analysis[12]. The essential clear sky estimated of GHI and DNI required for the operation of the clear sky detection algorithm were sourced from the Copernicus Atmosphere Monitoring Service (CAMS) solar radiation database [13], offering a high temporal resolution of 1-minute intervals.

Following the identification of clear sky periods, our next step was to validate the mode described in section 2.3 against actual irradiance measurements. Given the variability of atmospheric conditions beyond the inputs used in the Radiative Transfer (RT) model, discrepancies between modeled and measured GHI are anticipated. Previous research has typically adopted a fixed threshold over the clean sky (without clouds and aerosols) irradiance—often a 5% difference between measured GHI and modeled clean sky GHI—to delineate CEE (e.g.,[14,15]). However, recognizing that our clear sky model incorporates the effect of aerosols, its performance exhibits a dependency on the Solar Zenith Angle (SZA), we opted for an SZA-dependent threshold to refine our CEE identification process.

To establish this tailored threshold, we analyzed the distribution of differences between modeled clear sky GHI and actual measured GHI, focusing on their quantiles. Specifically, we utilized the 90th percentile of these differences as a preliminary threshold, which acknowledges the slight model performance variation with SZA. To articulate this relationship more precisely and derive a final threshold formula, we fitted a third-degree polynomial to the 90th percentiles plotted against SZA. The resulting equation for the threshold as a function of SZA is expressed as:

$$threshold(sza) = a + b \cdot sza + c \cdot sza^2 + d \cdot sza^3 \quad (1)$$

This methodological adjustment for an SZA-dependent threshold is aimed at enhancing the accuracy of CEE detection by aligning the threshold more closely with the empirical performance of the clear sky model across different SZAs.

In addition to the condition where the difference between the measured GHI and the modeled clear sky GHI must exceed the specified threshold, as determined by Equation 1, an additional criterion for a valid CEE occurrence is the presence of an unobstructed sun-disc. This incorporates direct observations of the solar disc's visibility into our analysis. Consequently, a further essential condition requires that the DNI exceed 120 W/m².

3. RESULTS AND DISCUSSION

3.1 Detection of clear sky conditions

Clear sky conditions were identified using the method proposed by Inman et al.[10], utilizing 1-minute measurements of GHI and DNI, along with their respective clear sky estimated from the CAMS solar radiation database. Figure 1 illustrates the time series of measured GHI (grey line) during the period from 3rd to 15th October 2017, alongside the corresponding clear sky periods detected in the measurements. In this example, the clear sky periods identified demonstrate the selected clear sky detection model's effective performance.

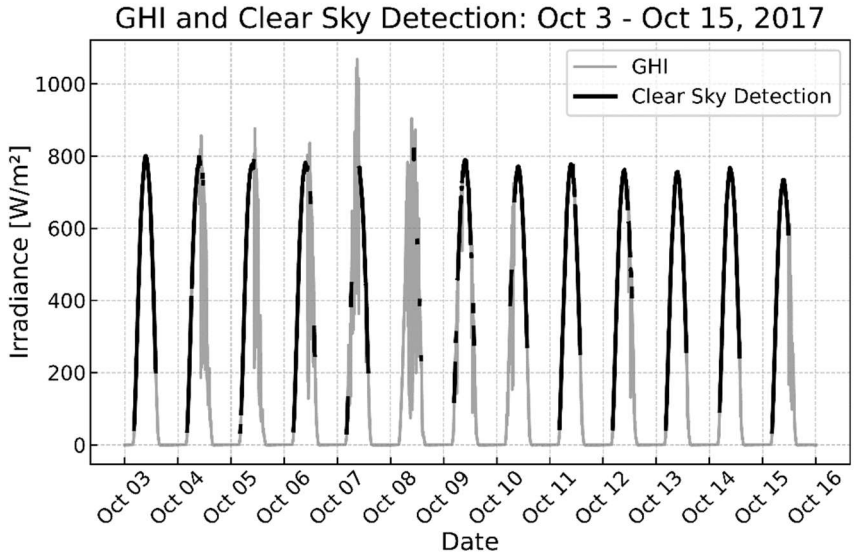

Figure 1: Visual representation of clear sky detection during the period 03-15/10/2017. Measured irradiance is in grey, and black thick line signifying minutes identified as clear.

3.2 Identification of enhancement events

To evaluate the performance of our clear sky model, it was compared with the measurement during the detected periods of clear sky conditions, as identified in section 3.1. Figure 2 presents a density scatter plot between the modelled clear sky GHI and the measured GHI for the detected clear sky conditions (a) and the histogram of the absolute differences between the two quantities. Although, they are highly correlated, displaying the model's ability to follow the patterns of GHI, there are some overestimations of the model. These discrepancies could be related to the inputs of the model, such as the aerosol properties or total precipitable water. Since overestimation is consistent, for the identification of the threshold for the definition of a CEE, this needs to be taken into consideration. Figure 3 shows the differences between the model and the measurements of GHI for clear sky conditions as a function of the SZA. Corresponding boxplot has been made for bins of 5 degrees SZA. To account for the model's overestimation, we assumed that the threshold for the identification of a CEE is when the difference of measured GHI and the modelled clear sky GHI is above the 90th quantile (q90). However, since the differences show a dependence from SZA, the 90th quantiles for each SZA bin was calculated and then a 3rd degree polynomial as a function of SZA was fitted, which is the final threshold (orange dashed line in Figure 3). Thus in order to have a CEE the measured GHI under all sky conditions minus the modelled clear sky GHI should as a function of SZA should be above the threshold identified by the orange dashed line. Taking as limit the q90 of the clear sky modelled GHI minus the measure GHI, we account for the overestimation in the modelled data, while introducing the SZA we take into account the different behavior for different SZAs. An additional critical factor in this analytical process is the requirement for DNI to be greater than 120 W/m², a criterion grounded in the World Meteorological Organization's (WMO) current threshold for sunshine duration[16].

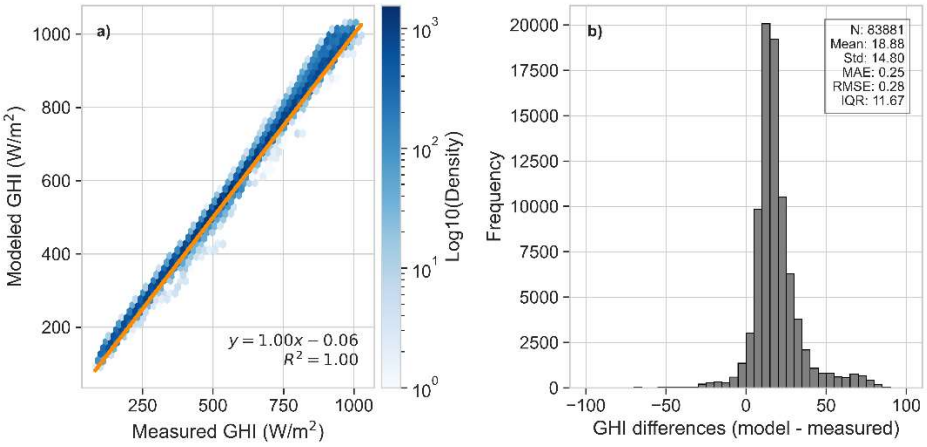

Figure 2: Density scatter plot of the modeled clear sky GHI versus the measurements for the detected clear sky conditions (a), and the distribution of the absolute differences between the modeled and measured GHI for clear sky conditions (b).

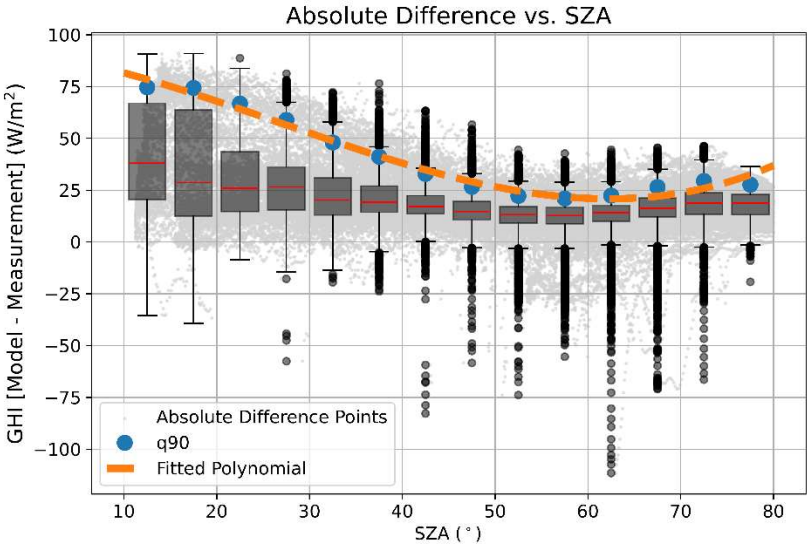

Figure 3: Absolute differences between the modeled and measured GHI for clear sky conditions as a function of SZA. The boxplots show the differences in bins of 5 degrees, the blue dots represent the 90th percentile (q90) of the differences, and the orange dashed line is a third-degree polynomial fit of the 90th percentiles as a function of SZA.

The time-series of the measured GHI, along with the respective modeled clear sky irradiance and the CEE as identified above is shown in Figure 4. The data illustrates the maximum recorded GHI of 1109 W/m² during the observation period. CEEs are discernible in 3.6% of total GHI measurements and are present on 49% of the days within our dataset, affirming their non-negligible contribution to solar irradiance. These results in close agreement with the ones reported in a similar study for Thessaloniki, Greece[17], although our dataset is limited to 6 months. However, the observed frequency of CEEs during the summer months is notably lower. This trend can be attributed to the scarcity of cloud cover over Limassol during this period[9,18]. The mean excess irradiance for CEEs is approximately 40 W/m², while the maximum observed enhancement reaches 264 W/m². These values suggest that during the autumn and winter months, the irradiance levels during CEEs approach or even surpass those typically observed in the summer months, indicating that CEEs can significantly alter the expected seasonal irradiance profile (Figure 4). Moreover, our analysis reveals instances where the measured GHI exceeds the total solar irradiance at the top of the atmosphere (TOA), adjusted for the horizontal plane, as

demonstrated in Figure 6. Out of the CEE occurrences cataloged, there are 24 cases—accounting for approximately 0.5% of all cases—where the GHI during a CEE surpasses the TOA levels.

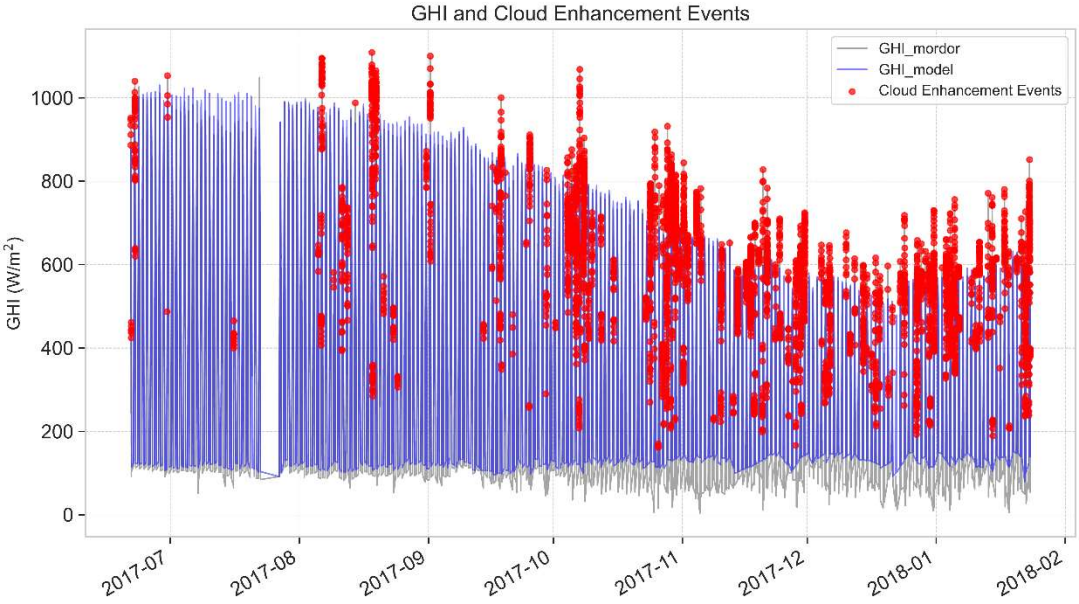

Figure 4: Time-series of the measured and clear sky modelled GHI, along with the irradiance enhancement events due to broken cloud conditions.

To further investigate the conditions under which CEE occur, we examined their distribution as a function of SZA and azimuth angle (Figure 5). The variation in CEE frequency with respect to SZA is indicative of the complex interplay between the sun's position and the atmospheric path length of sunlight. The data suggests an inhomogeneous distribution, with pronounced peaks at low SZAs where CEEs are significantly more frequent. This observation aligns with the hypothesis that certain atmospheric conditions—possibly characterized by cloud types with favorable edge geometry or specific aerosol concentrations—enhance the probability of CEEs through the optimal refraction and reflection of sunlight. However, there is a specific pattern of CEE appearance over specific azimuthal angles, which might suggest that the formation of clouds may happen over specific hours.

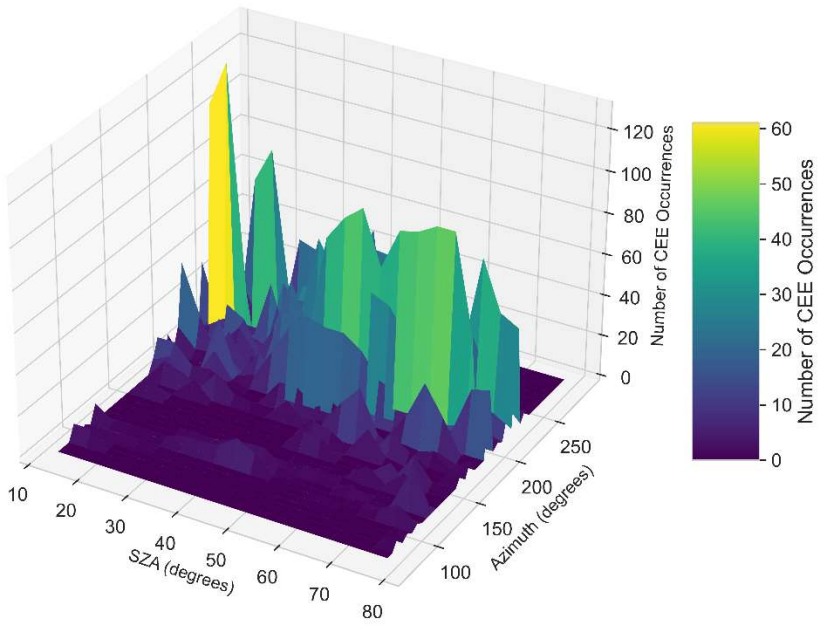

Figure 5: Three-Dimensional distribution of CEE frequencies as a function of solar zenith and azimuth angles.

3.3 Case study

Figure 6 illustrates the diurnal variability of GHI (depicted in blue) for October 7, 2017. Enhancement events, marked by red circles, denote instances where measured irradiance exceeded the threshold. The modeled clear sky GHI is represented by an orange dashed line, illustrating expected irradiance levels under clear sky conditions. The green line indicates the solar irradiance at the top of the atmosphere (TOA), adjusted for the horizontal plane. Notably, during the hours of 8 to 10 AM UTC, several instances were observed where the irradiance during a CEE surpassed the irradiance levels at the TOA, highlighting the significant impact of these events on solar irradiance.

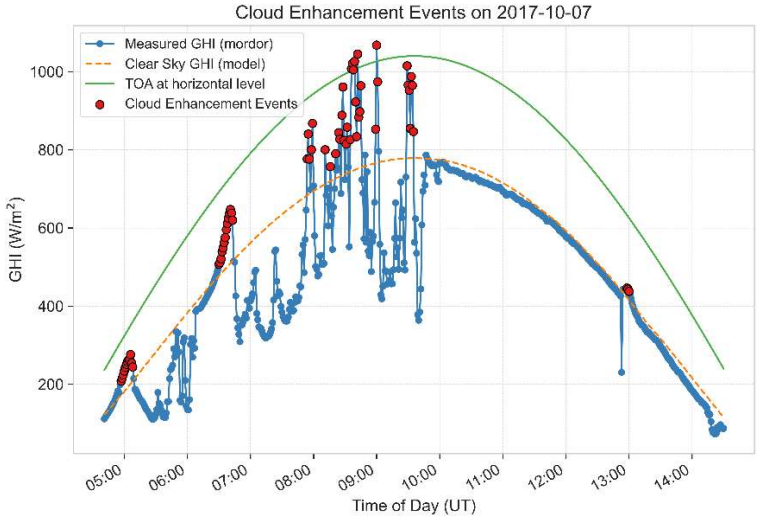

Figure 6: Diurnal variability of GHI (blue) for 2017-10-07. Red cycles denote the enhancement cases that were identified during the day. The orange dashed line represents the clear sky modelled GHI for this day, and the green line is the solar irradiance at the TOA, adjusted for the horizontal plane.

Presented in Figure 7 is the ACTRIS Cloudnet[19] target classification for October 7, 2017, elucidating the types of clouds present during the occurrence of the day's CEEs. It is evident that during the peak hours of CEEs (8-10 AM UTC), ice clouds extending from 4 to 6 kilometers were prevalent. The presence of these ice clouds is implicated in the enhanced reflection of solar irradiance, contributing to the observed over-irradiance events. This figure underscores the critical role of specific cloud formations in the amplification of solar irradiance at the surface, offering insights into the atmospheric conditions conducive to CEEs.

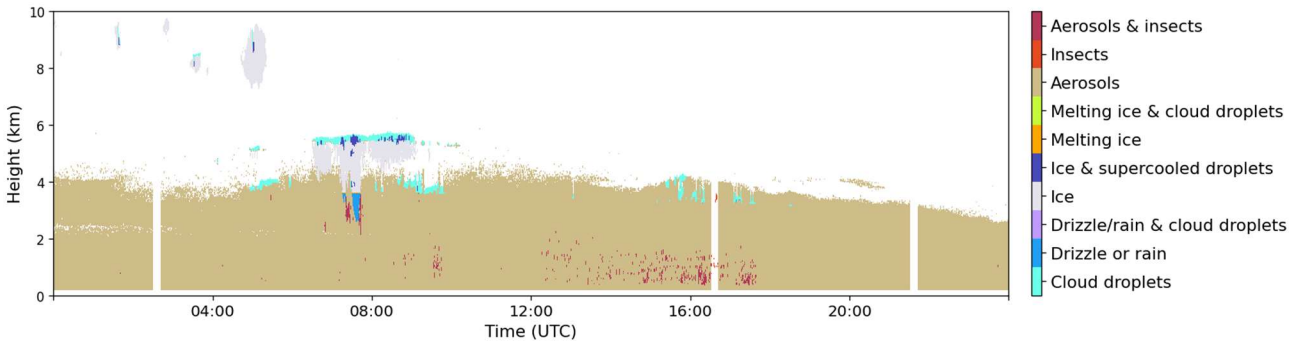

Figure 7: Cloudnet target classification for 2017-10-07.

4. CONCLUSIONS

This study has conducted a comprehensive statistical analysis of CEEs observed during the last six months of the Cy-CARE campaign in Limassol, Cyprus. Our findings indicate that, although solar irradiance enhancement events were detected on nearly half of the days with measurements, their occurrence during the summer months is markedly reduced due to the prevailing climatic conditions. Contrarily, during the autumn and winter months, CEEs can elevate GHI levels close or beyond those typically observed in summer, underscoring the significant impact of seasonal variations on solar irradiance. Further analysis revealed a predilection for CEEs to occur at specific solar azimuth angles, hinting at underlying patterns in cloud formation conducive to such events. This observation suggests a complex interplay between solar geometry and atmospheric conditions, meriting additional investigation beyond the scope of the current study. In exploring the nature of CEEs, we identified instances where measured GHI surpassed the irradiance at the TOA, adjusted for the horizontal plane. A detailed examination of one such case revealed that ice clouds, extending from 3 to 5 km in altitude, were instrumental in facilitating exceedances of TOA irradiance, presenting in six distinct instances. This correlation between cloud characteristics and the intensity of CEEs invites further research, particularly regarding the influence of cloud type and altitude on the occurrence and magnitude of these enhancement events.

The findings from this study not only contribute to our understanding of the factors influencing solar irradiance but also highlight the importance of considering atmospheric and cloud dynamics in solar energy forecasting. Future research aimed at dissecting the relationship between specific cloud formations and the propensity for CEEs could provide valuable insights for improving the accuracy of solar irradiance models and optimizing solar energy harvesting strategies.

ACKNOWLEDGEMENTS

"The authors acknowledge the 'EXCELSIOR': ERATOSTHENES: EXcellence Research Centre for Earth Surveillance and Space-Based Monitoring of the Environment H2020 Widespread Teaming project (www.excelsior2020.eu). The 'EXCELSIOR' project has received funding from the European Union's Horizon 2020 research and innovation programme under Grant Agreement No 857510, from the Government of the Republic of Cyprus through the Directorate General for the European Programmes, Coordination and Development and the Cyprus University of Technology".

REFERENCES

[1] Pfister, G., McKenzie, R. L., Liley, J. B., Thomas, A., Forgan, B. W. and Long, C. N., "Cloud coverage based on all-sky imaging and its impact on surface solar irradiance," Journal of Applied Meteorology **42**(10), 1421–1434 (2003).

[2] Järvelä, M., Lappalainen, K. and Valkealahti, S., "Characteristics of the cloud enhancement phenomenon and PV power plants," Solar Energy **196**, 137–145 (2020).

[3] Tapakis, R. and Charalambides, A. G., "Enhanced values of global irradiance due to the presence of clouds in Eastern Mediterranean," Renew Energy **62**, 459–467 (2014).

[4] do Nascimento, L. R., de Souza Viana, T., Campos, R. A. and Rüther, R., "Extreme solar overirradiance events: Occurrence and impacts on utility-scale photovoltaic power plants in Brazil," Solar Energy **186**, 370–381 (2019).

[5] Antón, M., Piedehierro, A. A., Alados-Arboledas, L., Wolfran, E. and Olmo, F. J., "Extreme ultraviolet index due to broken clouds at a midlatitude site, Granada (southeastern Spain)," Atmos Res **118**, 10–14 (2012).

[6] Radenz, M., Bühl, J., Seifert, P., Baars, H., Engelmann, R., Barja González, B., Mamouri, R.-E., Zamorano, F. and Ansmann, A., "Hemispheric contrasts in ice formation in stratiform mixed-phase clouds: disentangling the role of aerosol and dynamics with ground-based remote sensing," Atmos Chem Phys **21**(23), 17969–17994 (2021).

[7] Ansmann, A., Mamouri, R.-E., Bühl, J., Seifert, P., Engelmann, R., Hofer, J., Nisantzi, A., Atkinson, J. D., Kanji, Z. A., Sierau, B., Vrekoussis, M. and Sciare, J., "Ice-nucleating particle versus ice crystal number concentrationin altocumulus and cirrus layers embedded in Saharan dust:a closure study," Atmos Chem Phys **19**(23), 15087–15115 (2019).

[8] Emde, C., Buras-Schnell, R., Kylling, A., Mayer, B., Gasteiger, J., Hamann, U., Kylling, J., Richter, B., Pause, C., Dowling, T., Dowling, T. and Bugliaro, L., "The libRadtran software package for radiative transfer calculations (version 2.0.1)," Geosci Model Dev **9**(5), 1647–1672 (2016).

[9] Fountoulakis, I., Kosmopoulos, P., Papachristopoulou, K., Raptis, I.-P., Mamouri, R.-E., Nisantzi, A., Gkikas, A., Witthuhn, J., Bley, S., Moustaka, A., Kontoes, C. and Kazadzis, S., "Effects of aerosols and clouds on the levels of surface solar radiation and solar energy in cyprus," Remote Sens (Basel) **13**(12) (2021).

[10] Inman, R. H., Edson, J. G. and Coimbra, C. F. M., "Impact of local broadband turbidity estimation on forecasting of clear sky direct normal irradiance," Solar Energy **117** (2015).

[11] Bright, J. M., "Clear-sky Detection Library," https://github.com/JamieMBright/csd-library (2018).

[12] Gueymard, C. A., Bright, J. M., Lingfors, D., Habte, A. and Sengupta, M., "A posteriori clear-sky identification methods in solar irradiance time series: Review and preliminary validation using sky imagers," Renewable and Sustainable Energy Reviews **109** (2019).

[13] Lefèvre, M., Oumbe, A., Blanc, P., Espinar, B., Gschwind, B., Qu, Z., Wald, L., Schroedter-Homscheidt, M., Hoyer-Klick, C., Arola, A., Benedetti, A., Kaiser, J. W. and Morcrette, J. J., "McClear: A new model estimating downwelling solar radiation at ground level in clear-sky conditions," Atmos Meas Tech **6**(9) (2013).

[14] Vamvakas, I., Salamalikis, V. and Kazantzidis, A., "Evaluation of enhancement events of global horizontal irradiance due to clouds at Patras, South-West Greece," Renew Energy **151** (2020).

[15] Inman, R. H., Chu, Y. and Coimbra, C. F. M., "Cloud enhancement of global horizontal irradiance in California and Hawaii," Solar Energy **130** (2016).

[16] World Meteorological Organization., [Guide to Instruments and Methods of Observation: Measurement of meteorological variables-Volume I] (2018).
[17] Natsis, A., Bais, A. and Meleti, C., "A study of solar irradiance enhancement cases over Thessaloniki, Greece," AIP Conf Proc **2988**(1), 070002 (2024).
[18] Jacovides, C. P., Kaltsunides, N., Hachioannou, L. and Stefanou, L., "An assessment of the solar radiation climate of the Cyprus environment," Renew Energy **3**(8), 913–918 (1993).
[19] Illingworth, A. J., Hogan, R. J., O'Connor, E. J., Bouniol, D., Brooks, M. E., Delanoë, J., Donovan, D. P., Eastment, J. D., Gaussiat, N., Goddard, J. W. F., Wilson, D. R. and Wrench, C. L., "Cloudnet: Continuous evaluation of cloud profiles in seven operational models using ground-based observations," Bull Am Meteorol Soc **88**(6), 883–898 (2007).